Optical coherent injection of carrier and current in twisted bilayer graphene

Ze Zheng,[1,2] Ying Song,[1,2] Yu Wei Shan,[1,2] Wei Xin,[3] and Jin Luo Cheng[1,2,*]

[1]*GPL Photonics Lab, State Key Laboratory of Applied Optics, Changchun Institute of Optics, Fine Mechanics and Physics, Chinese Academy of Sciences, Changchun 130033, China*

[2]*University of Chinese Academy of Science, Beijing 100039, China*

[3]*Key Laboratory of UV-Emitting Materials and Technology, Ministry of Education, Northeast Normal University, Changchun 130024, China*

(Received 18 November 2021; revised 20 January 2022; accepted 21 January 2022; published 7 February 2022)

We theoretically investigate optical injection processes, including one- and two-photon carrier injection and two-color coherent current injection, in twisted bilayer graphene with moderate angles. The electronic states are described by a continuum model, and the spectra of injection coefficients are numerically calculated for different chemical potentials and twist angles, where the transitions between different bands are understood by the electron energy resolved injection coefficients. The comparison with the injection in monolayer graphene shows the significance of the interlayer coupling in the injection processes. For undoped twisted bilayer graphene, all spectra of injection coefficients can be divided into three energy regimes, which vary with the twist angle. For very low photon energies in the linear dispersion regime, the injection is similar to graphene with a renormalized Fermi velocity determined by the twist angle; for very high photon energies where the interlayer coupling is negligible, the injection is the same as that of graphene; and in the middle regime around the transition energy of the Van Hove singularity, the injection shows fruitful fine structures. Furthermore, the two-photon carrier injection diverges for the photon energy in the middle regime due to the existence of double resonant transitions.

DOI: 10.1103/PhysRevB.105.085407

I. INTRODUCTION

In recent years, twisted bilayer graphene (TBG) has attracted a great deal of attention in condensed matter physics as a novel platform for studying strong correlated phenomena [1–5], topological properties [6,7], chiralities [8,9], and nonlinear Hall effects [10]. The underlying physics arises from flat bands at certain "magic angles," implying strong carrier-carrier interactions. TBG is formed by the relative rotation of two-monolayer graphene at a twist angle θ [11,12]. After the rotation, the Dirac cones of these two layers intersect and form two saddle points, which further lead to the Van Hove singularities (VHS) in its density of states (DOS) or the joint density of states (JDOS) [13,14]. At the "magic angles," these two VHS merge to give flat bands [15,16]. The twist angle provides an additional degree of freedom to control the band structure, as well as the energy of VHS. For large twist angles, the band structure lower than VHS is mostly linear, similar to that of graphene but with a smaller Fermi velocity [17,18] that is determined by the twist angle.

The optical properties of TBG can be effectively tuned by the twist angle, and the optical transitions occurring around VHS are greatly enhanced, giving featured optical conductivity [17,19,20] and enhanced photoluminescence [21] for optoelectronic applications. The nonlinear optical properties of TBG have been extensively studied for second harmonic generation [22,23], third harmonic generation [24], third-order conductivity [25], high-harmonic generation [26,27], and nonlinear magneto-optic properties [28]. Compared to that of graphene, the huge nonlinear conductivity due to the resonance at VHS occurs at much lower photon energies, which might enable possible applications on nonlinear photonic devices at long wavelength. It is interesting to consider if other nonlinear optical phenomena can also benefit from such VHS enhanced transitions.

In this work, we focus on the two-color optical coherent injection of carriers and currents in TBG with twist angles limited in the range of 2°–10°, which are suitable for the continuum model we adopted and are easy to evaluate numerically. Two-color optical injection is a third-order nonlinear optical process, which utilizes the quantum interference between the optical excitation paths of the one-photon absorption by a weak light at frequency 2ω and degenerate two-photon absorption by a strong light at frequency ω. Both absorptions can generate electron-hole pairs and inject electrons in the conduction bands and holes in the valence bands; the interferences of these two absorption processes lead to net charge currents of injected carriers. Therefore, it can provide a full optical way to inject carriers and currents for studying their dynamics. Extensive investigations have been done for bulk semiconductors [29–32], topological materials [33], transition metal dichalcogenides [34], graphene [35–37], and bilayer graphene [36]. The difference between the results in graphene and bilayer graphene shows that the interlayer coupling has strong effects on the optical injection. In TBG, because the interlayer coupling can be effectively tuned by the twist angle, the optical injection is expected to be different from both the graphene and bilayer graphene, and it is possible to further understand the effects of interlayer

*jlcheng@ciomp.ac.cn

coupling on optical coherent control. This is the focus of this work.

We arrange the paper as follows. In Sec. II we introduce an effective model for TBG and expressions for injection coefficients. In Sec. III we present the main spectra features for the injection coefficients at a twist angle 4° as an example, we discuss the contributions from different electronic states using the electron energy resolved injection coefficients, and then we study the effects of chemical potentials and the twist angles. We conclude in Sec. IV.

II. MODELS

A. Electronic model Hamiltonian

TBG with a twist angle θ can be formed from rotating the upper and lower layers of AB-stacked bilayer graphene by angles of $-\frac{\theta}{2}$ and $\frac{\theta}{2}$ [15], respectively. The primitive reciprocal lattice vectors of the unrotated graphene layer are chosen as

$$\boldsymbol{b_1} = \frac{2\pi}{a_0}\begin{pmatrix}\frac{1}{\sqrt{3}}\\ -1\end{pmatrix}, \quad \boldsymbol{b_2} = \frac{2\pi}{a_0}\begin{pmatrix}\frac{1}{\sqrt{3}}\\ 1\end{pmatrix}, \tag{1}$$

and then the primitive reciprocal lattice vectors of TBG can be taken as

$$\boldsymbol{t_1} = R\left(-\frac{\theta}{2}\right)\boldsymbol{b_2} - R\left(\frac{\theta}{2}\right)\boldsymbol{b_2}, \tag{2}$$

$$\boldsymbol{t_2} = R\left(\frac{\theta}{2}\right)\boldsymbol{b_1} - R\left(-\frac{\theta}{2}\right)\boldsymbol{b_1}, \tag{3}$$

with the rotation matrix $R(\theta) = \left(\begin{smallmatrix}\cos\theta & -\sin\theta\\ \sin\theta & \cos\theta\end{smallmatrix}\right)$. After the rotation, the Dirac point $\boldsymbol{K} = (\boldsymbol{b_1} - \boldsymbol{b_2})/3$ of the unrotated layer is folded to TBG reciprocal space as the Dirac points $\boldsymbol{K_t} = (\boldsymbol{t_1} - 2\boldsymbol{t_2})/3$ from the upper layer and $\boldsymbol{K'_t} = (2\boldsymbol{t_1} - \boldsymbol{t_2})/3$ from the lower layer; similarly, the Dirac point $\boldsymbol{K'} = -\boldsymbol{K}$ of the unrotated layer is folded to TBG reciprocal space as $\boldsymbol{K'_t}$ and $\boldsymbol{K_t}$, respectively. These two valleys are decoupled. The low-energy electronic excitations around the νth valley ($\nu = +$ for the $\boldsymbol{K}$ point and $\nu = -$ for the $\boldsymbol{K'}$ point) of each graphene layer can be determined by a 4×4 continuum effective Hamiltonian [15],

$$H^{(\nu)}(\boldsymbol{\nabla}, \boldsymbol{r}) = \begin{pmatrix} h^{(\nu)}\left(-\frac{\theta}{2}, -i\boldsymbol{\nabla} - \nu\boldsymbol{K_t}\right) & T^{(\nu)}(\boldsymbol{r}) \\ [T^{(\nu)}(\boldsymbol{r})]^{\dagger} & h^{(\nu)}\left(\frac{\theta}{2}, -i\boldsymbol{\nabla} - \nu\boldsymbol{K'_t}\right)\end{pmatrix}, \tag{4}$$

where $h^{(\nu)}$ gives the graphene Hamiltonian in the νth valley as

$$h^{(\nu)}(\theta, \boldsymbol{k}) = \hbar v_f \begin{pmatrix} 0 & e^{i\nu\theta}(ik_x + \nu k_y) \\ e^{i\nu\theta}(-ik_x + \nu k_y) & 0\end{pmatrix}, \tag{5}$$

and $T^{(\nu)}(\boldsymbol{r})$ describes the interlayer coupling as

$$T^{(\nu)}(\boldsymbol{r}) = w_0\left(T_1^{(\nu)} + T_2^{(\nu)} e^{-i\nu\boldsymbol{t_1}\cdot\boldsymbol{r}} + T_3^{(\nu)} e^{-i\nu\boldsymbol{t_2}\cdot\boldsymbol{r}}\right), \tag{6}$$

with

$$T_1^{(\nu)} = \begin{pmatrix}1 & 1\\ 1 & 1\end{pmatrix}, \quad T_2^{(\nu)} = \begin{pmatrix} e^{i\nu\frac{2\pi}{3}} & 1 \\ e^{-i\nu\frac{2\pi}{3}} & e^{i\nu\frac{2\pi}{3}}\end{pmatrix},$$

$$T_3^{(\nu)} = \begin{pmatrix} e^{-i\nu\frac{2\pi}{3}} & 1 \\ e^{i\nu\frac{2\pi}{3}} & e^{-i\nu\frac{2\pi}{3}}\end{pmatrix}. \tag{7}$$

The parameter $v_f = \sqrt{3}\gamma_0 a_0/(2\hbar)$ is the Fermi velocity of graphene with $\gamma_0 = 3$ eV, and $w_0 = 110$ meV is the interlayer coupling strength. Obviously, the interlayer coupling potential $T^{(\nu)}(\boldsymbol{r})$ is periodic in space with primitive lattice vectors determined by the primitive reciprocal vectors $\boldsymbol{t_1}$ and $\boldsymbol{t_2}$. The continuum model adopted here is appropriate for twist angles less than or equal to 10°.

The Schrödinger equation in the νth valley becomes

$$H^{(\nu)}(\boldsymbol{\nabla}, \boldsymbol{r})\psi^{(\nu)}(\boldsymbol{r}) = E\psi^{(\nu)}(\boldsymbol{r}). \tag{8}$$

For a periodic potential, the eigen wave functions are Bloch states, and they can be expanded in plane waves as

$$\psi^{(\nu)}(\boldsymbol{r}) = \frac{1}{2\pi} e^{i\boldsymbol{k}\cdot\boldsymbol{r}} \sum_{nm} e^{i\nu\boldsymbol{t}_{nm}\cdot\boldsymbol{r}} C^{(\nu)}_{nm\boldsymbol{k}}, \tag{9}$$

with $\boldsymbol{t}_{nm} = n\boldsymbol{t}_1 + m\boldsymbol{t}_2$. The expansion coefficient $C^{(\nu)}_{nm\boldsymbol{k}}$ is a four-component column vector, which can be further written into a compact column vector $C^{(\nu)}_{\boldsymbol{k}}$ with elements $[C^{(\nu)}_{\boldsymbol{k}}]_{nm} = C^{(\nu)}_{nm\boldsymbol{k}}$. Then the eigenequation can be written as

$$H^{(\nu)}_{\boldsymbol{k}} C^{(\nu)}_{s\boldsymbol{k}} = \epsilon^{(\nu)}_{s\boldsymbol{k}} C^{(\nu)}_{s\boldsymbol{k}}, \tag{10}$$

where the subscript s labels the band, and the matrix elements of $H^{(\nu)}_{\boldsymbol{k}}$ between $(n_1 m_1)$ and $(n_2 m_2)$ are a 4×4 matrix,

$$\begin{aligned}\left[H^{(\nu)}_{\boldsymbol{k}}\right]_{n_1 m_1, n_2 m_2} =& \begin{pmatrix} h^{(\nu)}\left(-\frac{\theta}{2}, \boldsymbol{k} + \nu\boldsymbol{t}_{n_1 m_1} - \nu\boldsymbol{K_t}\right) & 0 \\ 0 & h^{(\nu)}\left(\frac{\theta}{2}, \boldsymbol{k} + \nu\boldsymbol{t}_{n_1 m_1} - \nu\boldsymbol{K'_t}\right)\end{pmatrix}\delta_{n_1,n_2}\delta_{m_1,m_2} \\ &+ w_0\begin{pmatrix} & T_1^{(\nu)} \\ \left(T_1^{(\nu)}\right)^* & \end{pmatrix}\delta_{n_1,n_2}\delta_{m_1,m_2} + w_0\begin{pmatrix} 0 & T_2^{(\nu)}\delta_{n_1,n_2-1} \\ \left(T_2^{(\nu)}\right)^*\delta_{n_1,n_2+1} & 0\end{pmatrix}\delta_{m_1,m_2} \\ &+ w_0\begin{pmatrix} 0 & T_3^{(\nu)}\delta_{m_1,m_2-1} \\ \left(T_3^{(\nu)}\right)^*\delta_{m_1,m_2+1} & 0\end{pmatrix}\delta_{n_1,n_2}.\end{aligned} \tag{11}$$

The in-plane velocity operator is calculated from $\boldsymbol{v}^{(\nu)}_{\boldsymbol{k}} = \hbar^{-1}\nabla_{\boldsymbol{k}} H^{(\nu)}_{\boldsymbol{k}}$, and its matrix elements between band eigenstates are

$$\boldsymbol{v}^{(\nu)}_{s_1 s_2 \boldsymbol{k}} = \left[C^{(\nu)}_{s_1\boldsymbol{k}}\right]^{\dagger} \boldsymbol{v}^{(\nu)}_{\boldsymbol{k}} C^{(\nu)}_{s_2\boldsymbol{k}}. \tag{12}$$

The time-reversal symmetry connects these two valleys $\nu = \pm$, and it can also be directly verified that

$$H^{(-)}_{\boldsymbol{k}} = \left[H^{(+)}_{-\boldsymbol{k}}\right]^*. \tag{13}$$

Therefore, we can always choose $C^{(-)}_{s\boldsymbol{k}} = [C^{(+)}_{s(-\boldsymbol{k})}]^*$ and $\epsilon^{(-)}_{s\boldsymbol{k}} = \epsilon^{(+)}_{s(-\boldsymbol{k})}$. Then the velocity matrix elements satisfy

$$\boldsymbol{v}^{(-)}_{s_1 s_2 \boldsymbol{k}} = -\boldsymbol{v}^{(+)}_{s_2 s_1 (-\boldsymbol{k})}. \tag{14}$$

B. Carrier injection and coherent current injection

We consider the two-color coherent control of injected carriers and currents in TBG induced by an electric field $\boldsymbol{E}(t) = \boldsymbol{E}_\omega e^{-i\omega t} + \boldsymbol{E}_{2\omega} e^{-2i\omega t} + \text{c.c.}$, where the 2ω beam is usually generated from the second harmonic of the ω beam. The injection of a physical quantity P can be described [37] by

$$\frac{dP(t)}{dt} = p_1^{ab}(\omega)\left[E^a_\omega\right]^* E^b_\omega + p_1^{ab}(2\omega)\left[E^a_{2\omega}\right]^* E^b_{2\omega} + p_2^{abcd}(\omega)\left[E^a_\omega\right]^*\left[E^b_\omega\right]^* E^c_\omega E^d_\omega + \left\{p_{12}^{abc}(\omega)\left[E^a_{2\omega}\right]^* E^b_\omega E^c_\omega + \text{c.c.}\right\}. \tag{15}$$

The first two terms involving $p_1^{ab}(\omega)$ describe the injection induced by one-photon absorption at photon frequencies ω and 2ω, respectively. The third term involving $p_2^{abcd}(\omega)$ describes the injection induced by degenerate two-photon absorption at photon frequency ω. When one-photon absorption at 2ω and two-photon absorption at ω occur simultaneously, the same electronic states can be optically excited to the same final electronic states by two different quantum paths, which lead to an interference, giving the coherent control of the injection. All these response coefficients can be derived from the Fermi golden rule [37,38], and they can be written as the sum of the contributions from two valleys $p = \sum_{\nu=\pm} p^{(\nu)}$ with

$$p_1^{(\nu);ab}(\omega) = 2 \times 2\pi \left(\frac{e}{\hbar\omega}\right)^2 \sum_{ss'} \int \frac{d\boldsymbol{k}}{(2\pi)^2} P^{(\nu)}_{ss'\boldsymbol{k}} \left(v^{(\nu);a}_{ss'\boldsymbol{k}}\right)^* v^{(\nu);b}_{ss'k} f^{(\nu)}_{s'sk} \delta\left(\omega^{(\nu)}_{ss'\boldsymbol{k}} - \omega\right), \tag{16}$$

$$p_2^{(\nu);abcd}(\omega) = 2 \times 2\pi \left(\frac{e}{\hbar\omega}\right)^4 \sum_{ss'} \int \frac{d\boldsymbol{k}}{(2\pi)^2} P^{(\nu)}_{ss'\boldsymbol{k}} \left(w^{(\nu);ab}_{ss'\boldsymbol{k}}\right)^* w^{(\nu);cd}_{ss'\boldsymbol{k}} f^{(\nu)}_{s'sk} \delta\left(\omega^{(\nu)}_{ss'\boldsymbol{k}} - 2\omega\right), \tag{17}$$

$$p_{12}^{(\nu);abc}(\omega) = -2 \times \pi i \left(\frac{e}{\hbar\omega}\right)^3 \sum_{ss'} \int \frac{d\boldsymbol{k}}{(2\pi)^2} P^{(\nu)}_{ss'\boldsymbol{k}} \left(v^{(\nu);a}_{ss'\boldsymbol{k}}\right)^* w^{(\nu);bc}_{ss'\boldsymbol{k}} f^{(\nu)}_{s'sk} \delta\left(\omega^{(\nu)}_{ss'\boldsymbol{k}} - 2\omega\right). \tag{18}$$

Here the superscripts a, b, c, d stand for the Cartesian directions x, y. The prefactor 2 comes from the spin degeneracy. $f^{(\nu)}_{s'sk} = f^{(\nu)}_{s'\boldsymbol{k}} - f^{(\nu)}_{s\boldsymbol{k}}$ gives the electron population difference, where $f^{(\nu)}_{s\boldsymbol{k}} = \Theta(\mu - \varepsilon^{(\nu)}_{s\boldsymbol{k}})$ is the Fermi-Dirac distribution at chemical potential μ and zero temperature, with Θ being the Heaviside step function, and the matrix elements $w^{(\nu);ab}_{ss'\boldsymbol{k}}$ are given as

$$w^{(\nu);ab}_{ss'\boldsymbol{k}} = \sum_m \frac{v^{(\nu);a}_{sm\boldsymbol{k}} v^{(\nu);b}_{ms'\boldsymbol{k}} + v^{(\nu);b}_{sm\boldsymbol{k}} v^{(\nu);a}_{ms'\boldsymbol{k}}}{\omega^{(\nu)}_{ms\boldsymbol{k}} + \omega^{(\nu)}_{ms'\boldsymbol{k}} - i\gamma}, \tag{19}$$

with $\hbar\omega^{(\nu)}_{ss'\boldsymbol{k}} = \epsilon^{(\nu)}_{s\boldsymbol{k}} - \epsilon^{(\nu)}_{s'\boldsymbol{k}}$. The quantity γ is a phenomenological damping parameter to avoid divergence.

In conventional semiconductors, the absorption processes for $p_1^{(\nu);ab}(\omega)$, $p_2^{(\nu);abcd}(\omega)$, and $p_{12}^{(\nu);abc}(\omega)$ can occur only when the photon energy $2\hbar\omega$ is larger than the band gap E_g. Because TBG has no band gap in our adopted model, these processes in principle can occur at any photon energy in an undoped TBG. However, when TBG is doped to a chemical potential μ, the population difference $f^{(\nu)}_{s'sk}$ leads to an absorption edge by Pauli blocking. This is equivalent to a chemical potential induced effective gap parameter E_g, which can set the injection edge. For small μ, it is the same as graphene with $E_g = 2|\mu|$.

For carrier injection, we set $P^{(\nu)}_{ss'\boldsymbol{k}} = 1$ and use symbols ξ_1 and ξ_2 as one- and two-photon injection coefficients; for current injection, we set $P^{(\nu)}_{ss'\boldsymbol{k}} = e(v^{(\nu);g}_{ss\boldsymbol{k}} - v^{(\nu);g}_{s's'\boldsymbol{k}})$ and use symbols η^g as injection coefficients. The injection coefficient ξ_1 is a second-order tensor, and ξ_2 and η are fourth-order tensors. The crystal symmetry of TBG depends on the initial stacking order and rotation center [15,39]. In our model, the point group of the structure is D_6. Thus the nonzero in-plane components [40] are $\xi_1^{xx} = \xi_2^{yy}$ for ξ_1^{ab}, $\xi_2^{xxxx} = \xi_2^{yyyy} = \xi_2^{xxyy} + 2\xi_2^{yxxy}$, $\xi_2^{xyxy} = \xi_2^{yyyx}$ for ξ_2^{abcd}, and similar results for η_{12}^{gabc}. By inspecting the expression in Eqs. (16)–(18), it can be found that $\xi_1^{ab} = [\xi_1^{ba}]^*$ and $\xi_2^{abcd} = [\xi_2^{cdab}]^*$, thus ξ_1^{xx}, ξ_2^{xxyy}, and ξ_2^{xyxy} are all real, and η_{12}^{xxyy} and η_{12}^{xyxy} are in general complex. Furthermore, there exists time-reversal symmetry linking the $\pm$ valleys. All injection coefficients can then be obtained from the calculation of one valley. For one-photon carrier injection, it gives $\xi_1^{(+);ab}(\omega) = \xi_1^{(-);ab}(\omega)$; for two-photon carrier injection and coherent current injection, we have

$$\xi_2^{abcd}(\omega) = 8\pi \left(\frac{e}{\hbar\omega}\right)^2 \sum_{ss'} \int \frac{d\boldsymbol{k}}{(2\pi)^2} f^{(+)}_{s'sk} \delta(\omega^{(+)}_{ss'\boldsymbol{k}} - 2\omega) \times \text{Re}\left[\left(w^{(+);ab}_{1;ss'\boldsymbol{k}}\right)^* w^{(+);cd}_{1;ss'\boldsymbol{k}} + \left(w^{(+);ab}_{2;ss'\boldsymbol{k}}\right)^* w^{(+);cd}_{2;ss'\boldsymbol{k}}\right], \tag{20}$$

$$\eta_{12}^{gabc}(\omega) = -4\pi \left(\frac{e}{\hbar\omega}\right)^3 \sum_{ss'} \int \frac{d\boldsymbol{k}}{(2\pi)^2} f^{(+)}_{s'sk} \delta(\omega^{(+)}_{ss'\boldsymbol{k}} - 2\omega) \times \left\{-i\text{Re}\left[\left(v^{(+);g}_{ss\boldsymbol{k}} - v^{(+);g}_{s's'\boldsymbol{k}}\right) v^{(+);a}_{s'sk} w^{(+);bc}_{1;ss'\boldsymbol{k}}\right] + \text{Im}\left[\left(v^{(+);g}_{ss\boldsymbol{k}} - v^{(+);g}_{s's'\boldsymbol{k}}\right) v^{(+);a}_{s'sk} w^{(+);bc}_{2;ss'}\right]\right\}, \tag{21}$$

with $w^{(\nu);ab}_{ss'\boldsymbol{k}} = w^{(\nu);ab}_{1;ss'\boldsymbol{k}} + iw^{(\nu);ab}_{2;ss'\boldsymbol{k}}$ and

$$w^{(\nu);ab}_{1;ss'\boldsymbol{k}} = \sum_m \frac{v^{(\nu);a}_{sm\boldsymbol{k}} v^{(\nu);b}_{ms'\boldsymbol{k}} + v^{(\nu);b}_{sm\boldsymbol{k}} v^{(\nu);a}_{ms'\boldsymbol{k}}}{\left(\omega^{(\nu)}_{ms\boldsymbol{k}} + \omega^{(\nu)}_{ms'\boldsymbol{k}}\right)^2 + \gamma^2} \left(\omega^{(\nu)}_{ms\boldsymbol{k}} + \omega^{(\nu)}_{ms'\boldsymbol{k}}\right), \quad (22)$$

$$w^{(\nu);ab}_{2;ss'\boldsymbol{k}} = \sum_m \frac{v^{(\nu);a}_{sm\boldsymbol{k}} v^{(\nu);b}_{ms'\boldsymbol{k}} + v^{(\nu);b}_{sm\boldsymbol{k}} v^{(\nu);a}_{ms'\boldsymbol{k}}}{\left(\omega^{(\nu)}_{ms\boldsymbol{k}} + \omega^{(\nu)}_{ms'\boldsymbol{k}}\right)^2 + \gamma^2} \gamma. \quad (23)$$

Here we give a brief discussion on the parameter γ. For graphene, which has only two bands in the simplest model, such a parameter can be taken as 0 directly because the denominator usually does not go to zero. However, due to the existence of many bands in TBG, the denominator in Eq. (19) can go to zero for zero γ when there exists an intermediate state in the middle of the initial and final states, i.e., $\epsilon^{(\nu)}_{s\boldsymbol{k}} + \epsilon^{(\nu)}_{s'\boldsymbol{k}} = 2\epsilon^{(\nu)}_{m\boldsymbol{k}}$. This condition leads to the resonant one-photon transition at ω between the initial and intermediate states; thus it requires the photon energy $2\hbar\omega > E_g$. To better understand how such divergences affect the injection coefficients, we show the limit of $\gamma \to 0$ in Eq. (23) as

$$\lim_{\gamma\to 0} w^{(\nu);ab}_{2;ss'\boldsymbol{k}} = \pi \sum_m \left(v^{(\nu);a}_{sm\boldsymbol{k}} v^{(\nu);b}_{ms'\boldsymbol{k}} + v^{(\nu);b}_{sm\boldsymbol{k}} v^{(\nu);a}_{ms'\boldsymbol{k}}\right) \times \delta\left(\omega^{(\nu)}_{ms\boldsymbol{k}} + \omega^{(\nu)}_{ms'\boldsymbol{k}}\right). \quad (24)$$

It gives an additional δ function. In the calculation of $\eta^{gabc}_{12}(\omega)$, the product of two δ functions $\delta(\omega^{(\nu)}_{ss'\boldsymbol{k}} - 2\omega)\delta(\omega^{(\nu)}_{ms\boldsymbol{k}} + \omega^{(\nu)}_{ms'\boldsymbol{k}})$ can behave well after integrating over two-dimensional wave vector $\boldsymbol{k}$, while in the calculation of $\xi^{abcd}_2(\omega)$, an additional product $\delta(\omega^{(\nu)}_{ss'\boldsymbol{k}} - 2\omega)[\delta(\omega^{(\nu)}_{ms\boldsymbol{k}} + \omega^{(\nu)}_{ms'\boldsymbol{k}})]^2$ appears and becomes divergent. However, this is physically meaningful: with the existence of the one-photon absorption, two-photon absorption is a signature toward saturated absorption. In this case a finite $\hbar\gamma = 10$ meV is adopted unless another value is specified, but one keeps in mind that the results depend strongly on the value of γ.

III. RESULTS AND DISCUSSION

In this work, we focus on the injection coefficients for twist angles between 3° and 10°. In the diagonalization of the Hamiltonian, the plane wave used for the wave-function expansion is taken as $e^{i\nu\boldsymbol{t}_{nm}\cdot\boldsymbol{r}}$ with $nm \in [-N, N][-N, N]$, and the numerical calculation of the injection coefficients is performed by discretizing the TBG Brillouin zone in an $M \times M$ grid. The δ function is approximated by a Gaussian function with an energy broadening 20 meV. The convergences of the results are checked with the values of N and M. At the twist angle 4°, we choose $N = 5$ and $M = 150$.

A. Band structure and density of states

As an example, we plot the band structure at $\theta = 4°$ in Fig. 1(a). The bands are labeled by $s = \pm1, \pm2, \ldots$, where negative/positive s are for bands with energies below/above zero. Together with the DOS shown in Fig. 1(b), the band structure clearly shows three energy regimes: (i) There exists a linear regime of the ±1 band around the Dirac points, which has already been well discussed and characterized by a renormalized Fermi velocity [15] $v'_f = \frac{1-3\alpha^2}{1+6\alpha^2} v_f$, with $\alpha = 3a_0 w_0/[8\pi v_f \sin(\theta/2)]$. It is easy to conclude that the physics in this regime should be similar to that of graphene, but with a smaller Fermi velocity and a larger DOS. At $\theta = 4°$, this regime is about in the energy range $[-0.19, 0.19]$ eV. (ii) When the electron energies are higher than 0.95 eV, the interlayer coupling shows little effect on the DOS. This is easy to understand because the coupling energy $w_0 = 110$ meV only contributes a bit to the electron energy in this case. The optical response of these two regimes is similar to the results of graphene. Because the continuum model for graphene is appropriate for electronic states in the linear dispersion regime (usually $< \gamma_0$), our calculation is performed for photon energy less than 5 eV. (iii) When the energy is between 0.19 and 0.95 eV, the band structure is complicated compared to that of graphene. There are multiple bands in this regime, and the M points of the ±1 bands [shown as red points in Figs. 1(a) and 1(b)] are saddle points, leading to VHS in the DOS at an energy of about 0.25 eV. The energies of these saddle points are approximately linear with the twist angle, as shown in Fig. 1(c). When the electron energy exceeds the VHS, there is a sudden decrease of the DOS, because the states are shifted to the M points to form VHS [19].

B. Injection coefficients at $\theta = 4°$

To clearly show how the interlayer coupling at different twist angles affects the injection, it is constructive to consider the ratio between the obtained results and those for uncoupled TBG, where the interlayer coupling strength is set as $w_0 = 0$. The uncoupled TBG becomes simply two uncoupled monolayers of graphene, and the injection occurs in each layer only, for which analytic results have been obtained [36]. The injec-

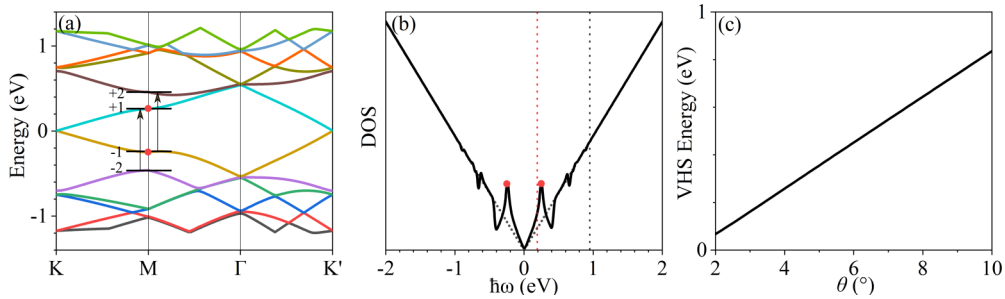

FIG. 1. Illustration of (a) the band structure and (b) the DOS for twist angle $\theta = 4°$. The two dotted vertical lines separate the three regimes in positive energies. (c) The twist angle dependence of energy at VHS.

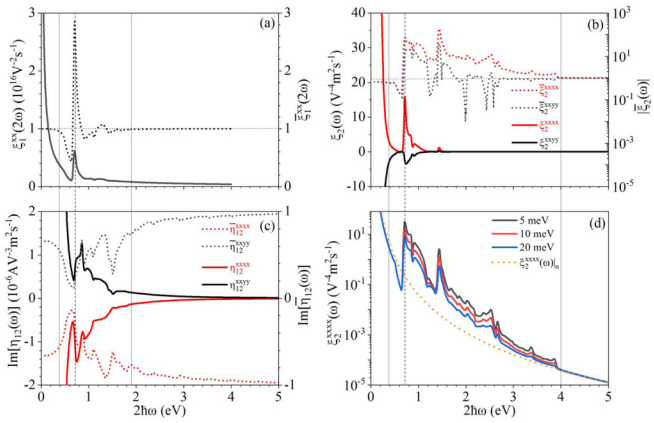

FIG. 2. Spectra of injection coefficients of TBG with $\theta = 4^\circ$ and $\mu = 0$. (a) One-photon carrier injection coefficient $\xi_1^{xx}(\omega)$, (b) two-photon carrier injection coefficients $\xi_2^{xxxx}(\omega)$ and $\xi_2^{xxyy}(\omega)$, and (c) the imaginary part of coherent current injection coefficients $\eta_{12}^{xxxx}(\omega)$ and $\eta_{12}^{xxyy}(\omega)$. In (a)–(c) the right axis gives the normalized injection coefficients. The vertical solid lines located at $2\hbar\omega = 0.38,\ 1.9$, or 4 eV divide the spectra into three regimes. The vertical dashed lines indicate the energy for the transition at the M point from band -1 (-2) to $+2$ ($+1$). (d) $\xi_2^{xxxx}(\omega)$ at different $\hbar\gamma = 5,\ 10,\ 20$ meV.

tion in graphene is isotropic with additional relations for the injection coefficients as $\xi_2^{xyxy} = -\xi_2^{xxyy}$ and $\eta_{12}^{xyxy} = -\eta_{12}^{xxyy}$. Thus in an uncoupled TBG for any twist angle θ, the injection coefficients are just twice those in graphene, as

$$\xi_1^{xx}(\omega)\Big|_u = \frac{e^2}{\hbar^2\omega}, \quad \xi_2^{xxxx}(\omega)\Big|_u = \frac{2\hbar v_f^2 e^4}{(\hbar\omega)^5},$$
$$\eta_{12}^{xxxx}(\omega)\Big|_u = i\frac{v_f^2 e^4}{(\hbar\omega)^3}. \tag{25}$$

The normalized injection coefficients are defined as $\bar{\xi}_1^{ab}(\omega) = \xi_1^{ab}(\omega)/\xi_1^{xx}(\omega)|_u$, $\bar{\xi}_2^{abcd}(\omega) = \xi_2^{abcd}(\omega)/\xi_2^{xxxx}(\omega)|_u$, and $\bar{\eta}_{12}^{gabc}(\omega) = \eta_{12}^{gabc}(\omega)/\mathrm{Im}[\eta_{12}^{gabc}(\omega)|_u]$, which are dimensionless quantities. In an uncoupled TBG, $\eta_{12}^{gabc}(\omega)$ is a pure imaginary number; with the inclusion of interlayer coupling, η_{12}^{gabc} is in general complex, but the calculations show that its real part is two orders of magnitude smaller than its imaginary part, which will be presented below. Figure 2 gives the spectra of these coefficients for a twist angle 4° at zero chemical potential. Corresponding to three regimes of the band structure, the spectra of injection coefficients can also be divided into three regimes, which are separated by $2\hbar\omega = 0.38$ and 1.9 eV for ξ_1^{ab} and η_{12}^{gabc} or $2\hbar\omega = 0.38$ and 4 eV for ξ_2^{abcd}. The second boundary is different due to the existence of unique divergence in two-photon absorption. At the low-energy regime $2\hbar\omega < 0.38$ eV, the injection occurs mostly between the bands ± 1 in the linear dispersion regime. The results are similar to those of graphene but with a smaller Fermi velocity v_f'. From Eq. (25), the one-photon injection coefficient is the same as the uncoupled TBG because it is independent of the Fermi velocity; however, two-photon carrier injection and two-color coherent current injection show smaller coefficients due to the smaller Fermi velocity. These features are clearly shown by the values $\bar{\xi}_1^{xx} = 1$, $\bar{\xi}_2^{xxxx}$, and $\bar{\eta}_{12}^{xxxx}$, which are approximately constant but less than 1. In the high-energy regime with photon energies $2\hbar\omega > 1.9$ eV for $\xi_1^{xx}(\omega)$ and $\eta_{12}^{xxxx}(\omega)$, or $2\hbar\omega > 4$ eV for $\xi_2^{xxxx}(\omega)$, the coefficients gradually approach the case without interlayer coupling.

In the middle regime, the spectra of injection coefficients contain fruitful fine structures, which are also clearly shown in the normalized injection coefficients. All of them have dips at $2\hbar\omega \approx 0.68$ eV, which are induced by the optical transitions involving the states with smaller DOS shown in Fig. 1(b). At $2\hbar\omega \approx 0.72$ eV, $\bar{\xi}_1^{xx}(\omega)$ appears as a peak with a value around 3, which arises from the optical transitions at the VHS. However, both $\bar{\eta}_{12}^{xxxx}(\omega)$ and $\bar{\eta}_{12}^{xxyy}(\omega)$ show local peaks at $2\hbar\omega = 0.76$ and 0.85 eV, respectively. The higher photon energies of these peak locations are because the VHS has zero carrier velocity $v_{s\boldsymbol{k}}^g - v_{s's'\boldsymbol{k}}^g$, which lowers and shifts the peak for current injection coefficients. After the peak, the injection coefficients decrease with some fine features (tiny dips), which are induced by the existence of multiple bands. In the whole middle regime, the normalized current injection coefficients are less than 1.

Different from one-photon carrier injection and two-color coherent injection, where the injection coefficients are at the same order of magnitude of graphene, the two-photon carrier injection can be a few hundred times larger than that of graphene for photon energies $0.72 < 2\hbar\omega < 4$ eV. This is because for these photon energies, both the resonant one-photon optical transition and the resonant two-photon optical transition can exist simultaneously, which leads to a double resonance discussed after Eq. (24). To better illustrate its dependence on γ, we also plot $\xi_2^{abcd}(\omega)$ in Fig. 2(d) for different $\hbar\gamma = 5,\ 10,\ 20$ meV. Our calculation indicates that the injection coefficients for the double resonant transitions are approximately proportional to γ^{-1}.

C. Electron energy resolved injection coefficients at $\theta = 4^\circ$

The injection processes can be better understood by using the electron energy resolved injection coefficients, from which the contributions from different electron energies can be visualized. As an example, for the one-photon injection, it is defined as

$$\tilde{\xi}_1^{(v);ab}(\epsilon_v, 2\omega) = 4\pi\left(\frac{e}{\hbar\omega}\right)^2 \sum_{ss'}\int \frac{d\boldsymbol{k}}{(2\pi)^2}\left(v_{ss'\boldsymbol{k}}^{(v);a}\right)^* v_{ss'k}^{(v);b} \times \delta(\varepsilon_{s'\boldsymbol{k}} - \epsilon_v)\hbar\delta(\varepsilon_{s\boldsymbol{k}} - \epsilon_v - 2\hbar\omega), \tag{26}$$

from which the injection coefficients can be obtained as

$$\xi_1^{(v);ab}(2\omega) = \int d\epsilon_v[\Theta(\mu - \epsilon_v) - \Theta(\mu - 2\hbar\omega - \epsilon_v)] \times \tilde{\xi}_1^{(v);ab}(\epsilon_v, 2\omega). \tag{27}$$

Similar definitions can be applied to get $\tilde{\xi}_2^{dabc}(\epsilon_v, \omega)$ and $\tilde{\eta}_{12}^{gabc}(\epsilon_v, \omega)$. Equation (27) shows that only the electron states with energies $\mu - 2\hbar\omega < \epsilon_v < \mu$ contribute to the injection process. For uncoupled TBG or for graphene, the injection occurs as $\epsilon_v = -\hbar\omega < -|\mu|$.

Figure 3 shows electron energy resolved injection coefficients $\tilde{\xi}_1^{xx}(\epsilon_v, 2\omega)$, $\tilde{\xi}_2^{xxxx}(\epsilon_v, \omega)$, and $\tilde{\eta}_{12}^{xxxx}(\epsilon_v, \omega)$. Taking $\tilde{\xi}_1^{xx}(\epsilon_v, 2\omega)$ as an example, the main contributions are located

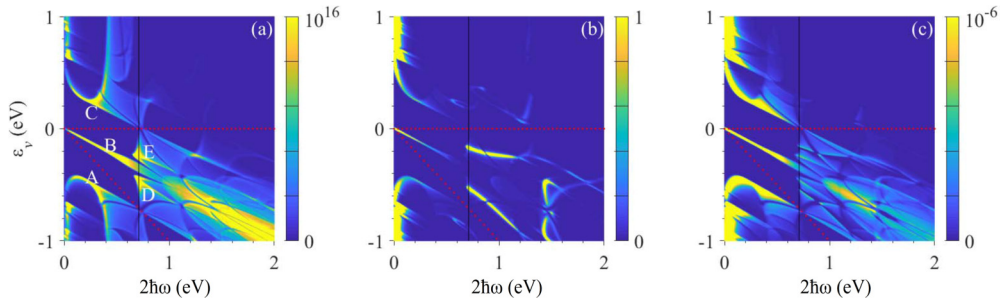

FIG. 3. Electron energy resolved injection coefficients (a) $(\frac{2\hbar\omega}{1\,\mathrm{eV}})^2\widetilde{\xi}_1^{xx}(\epsilon_v, 2\omega)$, (b) $(\frac{\hbar\omega}{1\,\mathrm{eV}})^4\widetilde{\xi}_2^{xxxx}(\epsilon_v, \omega)$, and (c) $(\frac{2\hbar\omega}{1\,\mathrm{eV}})^3\mathrm{Im}[\widetilde{\eta}_{12}^{xxxx}(\epsilon_v, \omega)]$. The two dotted lines give $\epsilon_v = \mu$ and $\epsilon_v = \mu - \hbar\omega$ for $\mu = 0$ eV.

in the regions identified by the optical transitions between bands A: $-2 \to -1$, B: $-1 \to 1$, C: $1 \to 2$, D: $-2 \to 1$, E: $-1 \to 2$, and F: for transitions from or to higher-energy bands. The regions D and E include the optical transitions around the VHS. At $\mu = 0$, the electron energy resolved injection coefficients are mostly located in the region $-2\hbar\omega < \epsilon_v < 0$ given by the dashed red lines, including the regions B, E, and D. For nonzero μ, contributions from other regions can be tuned on or off, which will be discussed in the next section.

D. Chemical potential dependence at $\theta = 4°$

Now we consider how doping affects the injection coefficients. Figure 4 shows the spectra for $\mu = 0,\ 0.1,\ 0.3,\ 0.5$ eV at 4°. For $\mu = 0.1$ eV, the chemical potential is in the linear dispersion regime. Following the results of graphene, the chemical potential induced effective band gap is $E_g = 2|\mu|$, thus all injection coefficients show an onset energy at $2\hbar\omega = 0.2$ eV. The new transitions from the $+1$ band to higher bands (from region C in Fig. 3) require higher photon energies and the contribution is negligible, so the results after the effective gap are almost the same as those results at zero chemical potential. When the chemical potential increases to 0.3 eV, which still lies in the $+1$ band, a direct consideration of the effective gap should be as high as 0.6 eV. However, the higher doping level makes transitions from the $+1$ band to higher bands (from region C in Fig. 3) require less photon energy, which reduces the effective gap to 0.15 eV. When the chemical potential is 0.5 eV, the onset energy becomes even smaller at around 0. From Fig. 3, all injections contributed from regions B, D, and E are suppressed, but region C contributes greatly for small photon energies, and it enhances the one-photon carrier injection for photon energies between 0.27 and 0.31 eV, and two-photon carrier injection and coherent current injection for photon energies between 0.27 and 0.5 eV.

E. Interference effects on current injection at $\theta = 4°$

To better illustrate how the injected current can be coherently controlled, we show the explicit dependence of the injection currents on light phases. Taking the electric fields as $\boldsymbol{E}_\omega = e^{i\phi_1}E_\omega\hat{\boldsymbol{e}}_\omega$ and $\boldsymbol{E}_{2\omega} = e^{i\phi_2}E_{2\omega}\hat{\boldsymbol{e}}_{2\omega}$, the injection current is written from Eq. (15) as

$$\frac{d\boldsymbol{J}}{dt} = -E_\omega^2 E_{2\omega}\{4\,\mathrm{Im}[\eta_{12}^{xyxy}]\mathrm{Im}[e^{i\Delta\phi}\hat{\boldsymbol{e}}_\omega\hat{\boldsymbol{e}}_{2\omega}^*\cdot\hat{\boldsymbol{e}}_\omega] + 2\,\mathrm{Im}[\eta_{12}^{xxyy}]\mathrm{Im}[e^{i\Delta\phi}\hat{\boldsymbol{e}}_{2\omega}^*\hat{\boldsymbol{e}}_\omega\cdot\hat{\boldsymbol{e}}_\omega]\}, \tag{28}$$

where $\Delta\phi = 2\phi_1 - \phi_2$ is the phase difference of these two beams. For collinearly polarized beams, the injection currents are zero for $\Delta\phi = 0$ or π but maximized for $\Delta\phi = \pm\pi/2$. Usually the interference can also be identified by a swarm velocity [38], which is an average velocity of excited carriers defined as

$$\boldsymbol{v}_{\mathrm{swarm}} = \frac{1}{e}\frac{\dot{\boldsymbol{J}}}{\dot{n}_1 + \dot{n}_2}. \tag{29}$$

When both fields are polarized along the x direction with a phase difference $-\pi/2$, the swarm velocity can be written as

$$v_{\mathrm{swarm}}^x = \frac{1}{e}\frac{2\,\mathrm{Im}[\eta_{12}^{xxxx}]E_\omega^2 E_{2\omega}}{\xi_1^{xx}E_{2\omega}^2 + \xi_2^{xxxx}E_\omega^4}. \tag{30}$$

It can be maximized at $E_\omega^2/E_{2\omega} = \sqrt{\xi_1^{xx}/\xi_2^{xxxx}}$. In Fig. 5, we show the $\boldsymbol{k}$-resolved carrier injection coefficients in one valley for the parameters $\hat{\boldsymbol{e}}_\omega = \hat{\boldsymbol{e}}_{2\omega} = \hat{\boldsymbol{x}}$, $2\hbar\omega = 0.4$ eV, and $E_\omega^2/E_{2\omega} \sim 4 \times 10^7$ V/m. When only one-photon or two-photon carrier absorption is considered, the $\boldsymbol{k}$-resolved in-

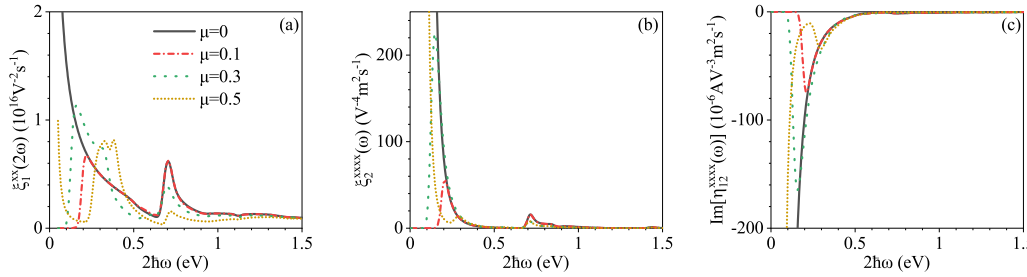

FIG. 4. Spectra of injection coefficients (a) $\xi_1^{xx}(2\omega)$, (b) $\xi_2^{xxxx}(\omega)$, and (c) $\mathrm{Im}[\bar{\eta}_{12}^{xxxx}(\omega)]$ for chemical potentials $\mu = 0,\ 0.1,\ 0.3,\ 0.5$ eV.

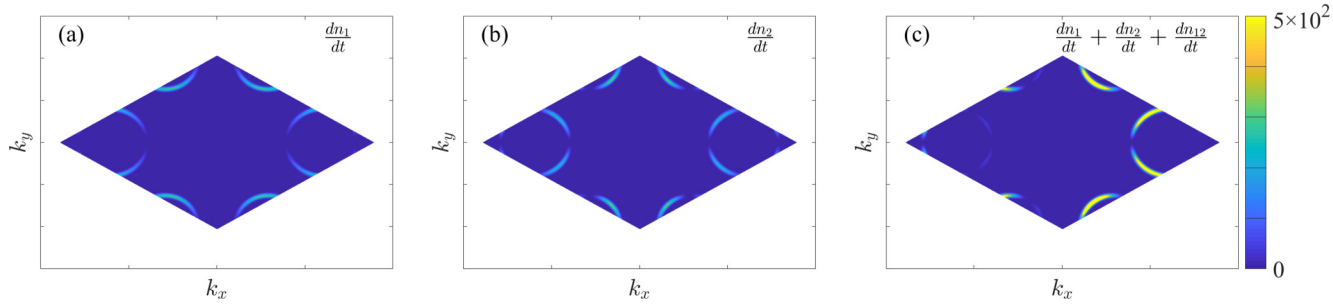

FIG. 5. Illustration of the interference by $\boldsymbol{k}$-resolved carrier injection coefficients: (a) one-photon carrier injection, (b) two-photon carrier injection, and (c) total carrier injection.

jection coefficients are symmetric, which leads to zero charge current. When the interference of these two absorptions is taken into account, the injection becomes clearly asymmetric and results in nonzero charge currents along the x direction.

We estimate the amplitude of the injection current using typical experimental parameters [35]. The fundamental laser beam is polarized along the y direction with wavelength 3.2 μm and intensity 2.8 GW/cm^2, while the second harmonic laser beam is polarized along the x direction with intensity 0.45 GW/cm^2. Their field amplitudes are about 10^7 V/m and 4×10^6 V/m, respectively. By taking pulse durations as $\Delta = 220$ fs, the phase difference as $\Delta\phi = -\pi/2$, and an electrode length as $l = 10$ μm, the injected current is estimated as $J \sim \frac{dJ}{dt} l\Delta = 2\,\mathrm{Im}[\eta_{12}^{xxyy}]E_\omega^2 E_{2\omega} l\Delta = 1.8$ mA with $\mathrm{Im}[\eta_{12}^{xxyy}] = 9.48\times10^{-7}\,\mathrm{A\,V^{-3}\,m^2\,s^{-1}}$.

F. Twist angle dependence

Figure 6 gives the injection coefficients at $\theta = 2^\circ$. Similar to the results at $\theta = 4^\circ$, the peak located around 0.2 eV originates from the VHS. The optical transitions involving the VHS and other bands occur at lower photon energies, resulting in some other peaks at photon energies below 1 eV. From the normalized injection coefficients, it can be seen that the high-energy regime appears at quite low photon energies, due to the smaller VHS energy at this twist angle. Furthermore, the peak values of the normalized coefficients induced by VHS are smaller than those at $\theta = 4^\circ$.

Figure 7 gives the normalized injection coefficients for $\theta = 3^\circ$, 5°, 7°, 9°, and 10°. For $\theta > 10^\circ$, the continuum model for electronic states is not suitable [15]. The spectra at different twist angles show very similar features to that of 4°. With increasing θ, the peaks/valleys are shifted to larger photon energies, which is consistent with our analysis of the band structure. These results indicate that optical injection processes can be effectively tuned by the twist angle.

IV. CONCLUSION

We have theoretically investigated one- and two-photon carrier injection and two-color coherent current injection in twisted bilayer graphene for twist angles between 3° and 10°, where the injection coefficients are numerically evaluated at zero temperature for different chemical potentials. Compared to the results for graphene, the spectra of injection coefficients in twisted bilayer graphene exhibit different features in three energy regimes: in the low-energy regime where the band structure is approximately linear, all injection coefficients have similar behaviors to that of graphene, but with a different amplitude determined by the renormalized Fermi velocity; for very high photon energies, all injection coefficients are almost the same as that of graphene, because the involved electronic states have large energies that are not effectively affected by the interlayer coupling; and in the middle regime, the carrier injection coefficients show resonant peaks around the Van Hove singularity, while the current injection coefficients are smaller because the injected carriers around the Van Hove singularity have zero velocity. All these results are characterized by electron energy resolved injection coefficients. Due to the existence of multiple bands, the degenerate two-photon optical transition processes can have double resonant optical transitions between the initial, the intermediate, and the final states, which lead to a divergent two-photon carrier injection and a finite two-color current injection.

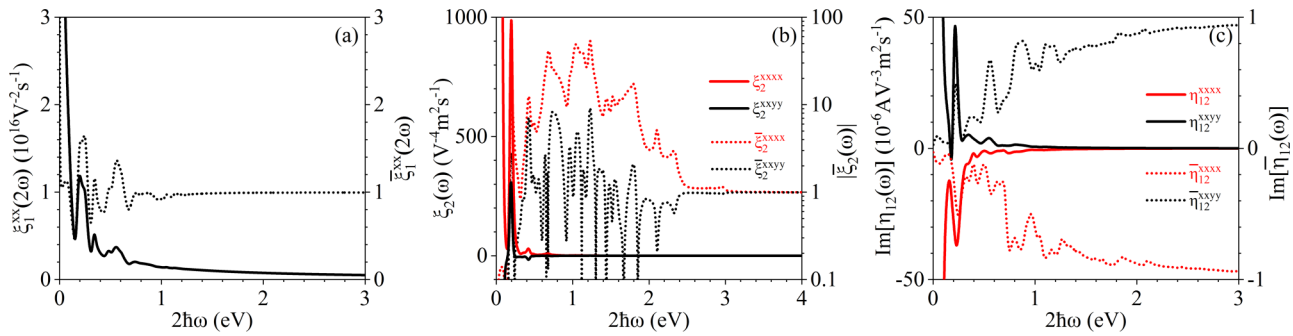

FIG. 6. Spectra of injection coefficients of TBG with $\theta = 2^\circ$ and $\mu = 0$.

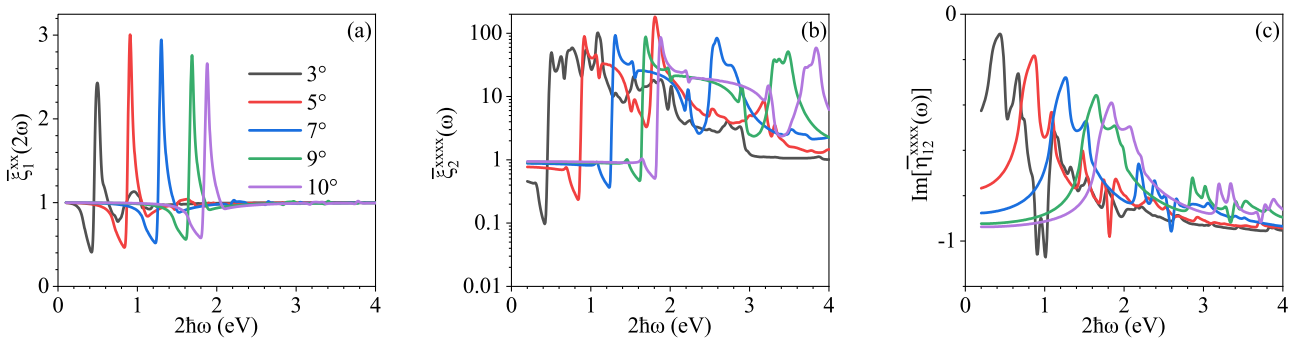

FIG. 7. Photon energy dependence of the normalized injection coefficients. (a) $\bar{\xi}_1^{xx}(\omega)$, (b) $\bar{\xi}_2^{xxxx}(\omega)$, and (c) $\mathrm{Im}[\eta_{12}^{xxxx}(\omega)]$ for different twist angles 3°, 5°, 7°, 9°, and 10°.

With the decrease of the twist angle, these features shift to low photon energies, suggesting twist angle tunable applications in far-infrared or terahertz wavelength. The optical injection for very small twist angles around the "magic angles" is not investigated in this work, mainly due to the difficulties in the numerical calculations, which require a large number of plane-wave expansions to get accurate band eigenstates and an inclusion of many higher intermediate bands to get the accurate amplitude for the two-photon transition process. However, at these angles, the strong carrier-carrier interaction may lead to a different behavior of the optical injection [31], which is worthwhile for future exploration.

This work mostly focuses on the comparison of the injection coefficients of twisted bilayer graphene and those of graphene, and there also exist other important injection processes appearing only in twisted bilayer graphene, which are worthy of being explored but are not discussed here. For example, the stacking of two layers of graphene brings the focus along the perpendicular direction [41], which is usually ignored in monolayer graphene, and the two-color optical injection tensors have nonzero components for oblique incident light. Moreover, due to the lower symmetry, a single color light with an appropriate polarization is also possible to inject currents.

ACKNOWLEDGMENTS

This work has been supported by a scientific research project of the Chinese Academy of Sciences, Grant No. QYZDB-SSW-SYS038, and by National Natural Science Foundation of China Grants No. 11774340, No. 12034003, No. 12004379, and No. 11804334. J.L.C. acknowledges the support from Talent Program of CIOMP.

[1] Y. Cao, V. Fatemi, S. Fang, K. Watanabe, T. Taniguchi, E. Kaxiras, and P. Jarillo-Herrero, Nature (London) **556**, 43 (2018).
[2] Y. Cao, V. Fatemi, A. Demir, S. Fang, S. L. Tomarken, J. Y. Luo, J. D. Sanchez-Yamagishi, K. Watanabe, T. Taniguchi, E. Kaxiras *et al.*, Nature (London) **556**, 80 (2018).
[3] U. Mogera and G. U. Kulkarni, Carbon **156**, 470 (2020).
[4] A. Nimbalkar and H. Kim, Nano-Micro Lett. **12**, 1 (2020).
[5] E. Y. Andrei and A. H. MacDonald, Nat. Mater. **19**, 1265 (2020).
[6] A. L. Sharpe, E. J. Fox, A. W. Barnard, J. Finney, K. Watanabe, T. Taniguchi, M. Kastner, and D. Goldhaber-Gordon, Science **365**, 605 (2019).
[7] A. L. Sharpe, E. J. Fox, A. W. Barnard, J. Finney, K. Watanabe, T. Taniguchi, M. A. Kastner, and D. Goldhaber-Gordon, Nano Lett. **21**, 4299 (2021).
[8] C.-J. Kim, A. Sánchez-Castillo, Z. Ziegler, Y. Ogawa, C. Noguez, and J. Park, Nat. Nano. **11**, 520 (2016).
[9] E. S. Morell, L. Chico, and L. Brey, 2D Mater. **4**, 035015 (2017).
[10] C.-P. Zhang, J. Xiao, B. T. Zhou, J.-X. Hu, Y.-M. Xie, B. Yan, and K. T. Law, arXiv:2010.08333.
[11] J. M. B. Lopes dos Santos, N. M. R. Peres, and A. H. Castro Neto, Phys. Rev. Lett. **99**, 256802 (2007).
[12] A. O. Sboychakov, A. L. Rakhmanov, A. V. Rozhkov, and F. Nori, Phys. Rev. B **92**, 075402 (2015).
[13] G. Li, A. Luican, J. M. B. L. Dos Santos, A. H. C. Neto, A. Reina, J. Kong, and E. Y. Andrei, Nat. Phys. **6**, 109 (2010).
[14] W. Yan, M. Liu, R.-F. Dou, L. Meng, L. Feng, Z.-D. Chu, Y. Zhang, Z. Liu, J.-C. Nie, and L. He, Phys. Rev. Lett. **109**, 126801 (2012).
[15] R. Bistritzer and A. H. MacDonald, Proc. Natl. Acad. Sci. (USA) **108**, 12233 (2011).
[16] E. Y. Andrei, D. K. Efetov, P. Jarillo-Herrero, A. H. MacDonald, K. F. Mak, T. Senthil, E. Tutuc, A. Yazdani, and A. F. Young, Nat. Rev. Mater. **6**, 201 (2021).
[17] C. J. Tabert and E. J. Nicol, Phys. Rev. B **87**, 121402(R) (2013).
[18] L.-J. Yin, J.-B. Qiao, W.-X. Wang, W.-J. Zuo, W. Yan, R. Xu, R.-F. Dou, J.-C. Nie, and L. He, Phys. Rev. B **92**, 201408(R) (2015).
[19] P. Moon and M. Koshino, Phys. Rev. B **87**, 205404 (2013).
[20] K. Yu, N. Van Luan, T. Kim, J. Jeon, J. Kim, P. Moon, Y. H. Lee, and E. J. Choi, Phys. Rev. B **99**, 241405(R) (2019).
[21] H. Patel, L. Huang, C.-J. Kim, J. Park, and M. W. Graham, Nat. Commun. **10**, 1 (2019).
[22] F. Yang, W. Song, F. Meng, F. Luo, S. Lou, S. Lin, Z. Gong, J. Cao, E. S. Barnard, E. Chan *et al.*, Matter **3**, 1361 (2020).
[23] S. J. Brun and T. G. Pedersen, Phys. Rev. B **91**, 205405 (2015).

[24] S. Ha, N. H. Park, H. Kim, J. Shin, J. Choi, S. Park, J.-Y. Moon, K. Chae, J. Jung, J.-H. Lee *et al.*, Light: Sci. Appl. **10**, 19 (2021).
[25] J. W. Zuber and C. Zhang, Phys. Rev. B **103**, 245417 (2021).
[26] T. N. Ikeda, Phys. Rev. Research **2**, 032015(R) (2020).
[27] M. Du, C. Liu, Z. Zeng, and R. Li, Phys. Rev. A **104**, 033113 (2021).
[28] J. Liu and X. Dai, npj Comput. Mater. **6**, 1 (2020).
[29] R. Atanasov, A. Haché, J. L. P. Hughes, H. M. van Driel, and J. E. Sipe, Phys. Rev. Lett. **76**, 1703 (1996).
[30] A. Haché, Y. Kostoulas, R. Atanasov, J. L. P. Hughes, J. E. Sipe, and H. M. van Driel, Phys. Rev. Lett. **78**, 306 (1997).
[31] R. D. R. Bhat and J. E. Sipe, Phys. Rev. B **72**, 075205 (2005).
[32] J. L. Cheng, J. Rioux, and J. E. Sipe, Phys. Rev. B **84**, 235204 (2011).
[33] R. A. Muniz and J. E. Sipe, Phys. Rev. B **89**, 205113 (2014).
[34] Q. Cui and H. Zhao, ACS Nano **9**, 3935 (2015).
[35] D. Sun, C. Divin, J. Rioux, J. E. Sipe, C. Berger, W. A. de Heer, P. N. First, and T. B. Norris, Nano Lett. **10**, 1293 (2010).
[36] J. Rioux, G. Burkard, and J. E. Sipe, Phys. Rev. B **83**, 195406 (2011).
[37] J. Rioux, J. E. Sipe, and G. Burkard, Phys. Rev. B **90**, 115424 (2014).
[38] H. M. van Driel and J. E. Sipe, *Ultrafast Phenomena in Semiconductors* (Springer, New York, 2001), pp. 261–306.
[39] M. Koshino, N. F. Q. Yuan, T. Koretsune, M. Ochi, K. Kuroki, and L. Fu, Phys. Rev. X **8**, 031087 (2018).
[40] R. W. Boyd, *Nonlinear Optics*, 3rd ed. (Academic, Florida, 2008).
[41] Y. Gao, Y. Zhang, and D. Xiao, Phys. Rev. Lett. **124**, 077401 (2020).